Late Winter Observations of Sea Ice Pressure Ridge Sail Height

Kyle Duncan, Sinead L. Farrell, Jennifer Hutchings, and Jacqueline Richter-Menge

Abstract—Analysis of high-resolution imagery acquired by the Digital Mapping System during annual, late-winter NASA Operation IceBridge surveys of Arctic sea ice between 2010 and 2018 reveals that pressure ridge sail heights (H_S) vary regionally and interannually. We find distinct differences in H_S distributions between the central Arctic (CA) and the Beaufort/Chukchi Seas region. Our results show that differences with respect to ice type occur within the tails of the H_S distributions and that the 95th and 99th percentiles of H_S are strong indicators of the predominant ice type in which the pressure ridge formed. During the first part of the study period H_S increased, with the largest sails observed in the winters of 2015 and 2016, after which H_S declined, suggesting that the most heavily deformed sea ice may have drifted beyond the area surveyed and exited the CA. Our analysis of the interannual and regional variability in sea ice deformation in the western Arctic during the last decade provides an improved understanding of sail height that will help advance ridge parameterizations in sea ice models.

Index Terms—Optical imagery, pressure ridge, sea ice.

I. Introduction

THE drift velocity and thickness of Earth's sea ice cover are considered essential climate variables, which provide the necessary evidence to understand the evolution of the climate system and guide mitigation and adaptation measures. Pressure ridges in the sea ice cover, formed by collision of drifting ice floes [1], or through compression of floes against land-fast ice (e.g., stamuki) and coastlines, play an important role in the mass and energy budgets of the polar oceans. Pressure ridge sails (that part of the ridge above the local sea ice surface) resist the movement of air over the ice surface, causing form drag [2], and are related to the thickness of the parent sea-ice sheet [3]. Widespread observations of pressure ridges, and the regional and temporal variability in their sail height, are vital for understanding the observed increase in sea ice drift [4] and concurrent decline in sea ice thickness in the Arctic.

Previous studies have used optical imagery to derive sail heights in small regions of the Arctic (e.g., [5]–[8]), but the methodology has yet to be applied across the basin. Here, we build upon that work, but at a larger, Arctic-wide scale, using the geographical coverage afforded by NASA's Operation IceBridge (OIB) surveys [9]. We present results describing sea ice pressure ridge sail height across the Arctic Ocean toward the end of the winter growth season, over a nine-year period (2010–2018). Sail heights are derived by measuring the length of shadows cast by pressure ridges, as observed in high-resolution Digital Mapping System (DMS) visible imagery gathered during OIB flights over sea ice. We assess interannual variability in sail height within two regions sampled by OIB and delineate results with respect to the predominant ice type in these regions.

II. Airborne Data

We utilize level-1B (IODMS1B) DMS geoTIFF data [10] acquired during annual OIB winter campaigns in the months of March, April, and May, between 2010 and 2018. The DMS is a 21-Mpixel Canon digital camera which provides high-resolution, red–green–blue (RGB or true color) imagery. DMS imagery has a spatial resolution of ∼0.1 m when acquired at the nominal OIB flight altitude of 450 m and represents an area of ∼650 m × 420 m on the Earth's surface. Images have been geolocated and orthorectified using an Applanix POS/AV orientation system. Boresight angles and lens distortion corrections have been applied in the creation of the final geoTIFF images to increase geolocation accuracy [10]. DMS data were filtered based on aircraft pitch and roll, and images acquired under adverse conditions (i.e., pitch and roll <−5° and >5°) were removed so as to limit the analysis to near nadir-pointing imagery.

III. Sail Height Extraction From DMS

Shadows cast by pressure ridges are easily identifiable in DMS images due to low solar elevation angles in March–May, and the sharp contrast between the shadow and the brighter sea ice surface [Fig. 1(a)], especially within the red channel of the image. Following the methodology of [8], we delineate shadow pixels from sea ice pixels to create a binary image mask. Shadow lengths [Fig. 1(b)] are calculated column-wise, from top to bottom and left to right, across the masked binary image.

Kyle Duncan is with the Cooperative Institute for Satellite Earth System Studies, University of Maryland, College Park, MD 20740 USA (e-mail: kyle.duncan@noaa.gov).

Sinead L. Farrell is with the Department of Geographical Sciences, University of Maryland, College Park, MD 20740 USA, and also with the Cooperative Institute for Satellite Earth System Studies, University of Maryland, College Park, MD 20740 USA.

Jennifer Hutchings is with the College of Earth, Ocean, and Atmospheric Sciences, Oregon State University, Corvallis, OR 97331 USA.

Jacqueline Richter-Menge is with the Institute of Northern Engineering, University of Alaska Fairbanks, Fairbanks, AK 99775 USA.
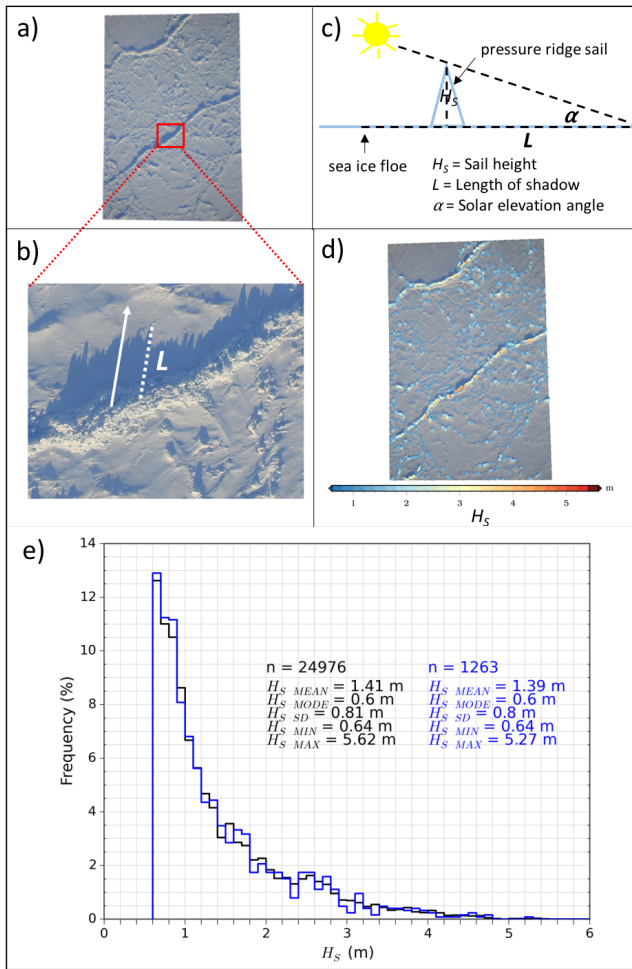
Fig. 1. Schematic showing methodology to derive sea ice pressure ridge sail height (H_S) from a single DMS image. (a) April 3, 2015 DMS image of Arctic sea ice (located at 77.266°N, −120.428°W), with linear pressure ridges. (b) Closeup of shadows cast by a pressure ridge, with direction of solar illumination (white arrow) and shadow length (white dashed line, L) shown. (c) Geometry used for derivation of H_S relative to local sea ice surface, based on shadow length (L) and direction and elevation of solar illumination (α). (d) Same DMS image as in (a), overlain with derived H_S. (e) Full H_S distribution (black) with statistics for $n = 24976$ individual H_S measurements shown in (d), and the reduced H_S distribution (blue) with statistics for $n = 1263$ H_S measurements, acquired from every 20th column of measurements shown in (d).

To speed up processing, shadow lengths are only calculated for every 20th column in the binary mask, resulting in ~1000 sail height measurements per image, depending on ice conditions. Shadow lengths (L), along with the image pixel size (S_P) and the solar elevation angle (α) at the time of image acquisition, are used to calculate the ridge sail height [H_S, Fig. 1(c)] as follows:

$$H_S = (L \cdot S_P) \cdot \tan(\alpha). \tag{1}$$

Minimum H_S was set at 0.6 m to exclude measurements of shadows cast by smaller-amplitude snow features (e.g., snow dunes) on the sea ice surface [8]. H_S is calculated for all pressure ridge features per DMS image [Fig. 1(d)], resulting in one distribution of sail heights [Fig. 1(e)] per image, from which a number of statistics can be derived, including the number of measurements (n); mean ($H_{S\ MEAN}$); mode ($H_{S\ MODE}$); minimum ($H_{S\ MIN}$); maximum ($H_{S\ MAX}$); standard deviation

($H_{S\ SD}$); and the 5th ($H_{S\ 5}$), 25th ($H_{S\ 25}$), 75th ($H_{S\ 75}$), 95th ($H_{S\ 95}$), and 99th ($H_{S\ 99}$) percentiles of H_S. Using every 20th column of the binary mask is shown to have little effect on the overall distribution of H_S per image when compared with using all columns [blue versus black curves, respectively, Fig. 1(e)]. Additional statistics are calculated over 25-km-long segments to reduce the impact of small-scale ice surface variability. Each 25 km segment can contain 50 images, but this depends on polar darkness conditions, or the presence of clouds or leads. On average, there are ~28 images per segment. We note that at the segment scale, $H_{S\ MAX}$ is derived from a single H_S measurement, while $H_{S\ 95}$ and $H_{S\ 99}$ are derived from the full H_S distribution across 25 km, and are thus more robust indicators of maximum H_S. We assess the predominant ice type within which the pressure ridge has formed. Numerous methodologies exist to derive ice type from satellite radar backscatter and/or passive microwave radiometer observations (e.g., [11]). In the following analysis, we use the daily sea ice-type product of the European Organisation for the Exploitation of Meteorological Satellites (EUMETSAT) Ocean and Sea Ice Satellite Application Facility (OSI SAF), OSI-403-c [12]. Distinguishing between multiyear ice (MYI), which has survived at least one summer melt season, and first-year ice (FYI) that has grown and melted within one year, indicates the age and thickness of the ice cover.

A. Image Preprocessing

Prior to processing, quality control was performed to separate images used in the analysis from those obscured by clouds, polar darkness, or contaminated with sea ice leads. During the late-winter OIB sea ice campaigns between 2010 and 2018, a total of 156 749 DMS images were acquired Of these, 67 720 (43.2%) were used for analysis, 70 493 (45%) were obscured by polar darkness and/or clouds, and 18 536 (11.8%) were discarded due to contamination by sea ice leads which are difficult to distinguish from ridge shadows (annual statistics provided in supplementary Fig. S1).

IV. CROSS-ARCTIC TRANSECT RESULTS

A variety of OIB surveys were flown across gradients in ice type. These were examined to determine if sail height was related to ice type. The following is an example of that analysis.

On April 20, 2016, an OIB survey known as the "Laxon Line" was flown from Thule Air Base, Greenland, to Fairbanks, Alaska, transiting across the Arctic Ocean [Fig. 2(a)]. Measurements of H_S were obtained over thick, predominantly MYI in the central Arctic (CA), and thinner, predominantly FYI in the Beaufort Sea. The transect also crossed over discrete MYI floes close to the northern coast of Alaska. The sail height was examined along the flight line transect to determine the relationship between the sail height and the predominant ice type. Sail height statistics were calculated for 25-km-long segments along the transect [Fig. 2(b)]. Slight changes were observed in $H_{S\ MEAN}$, $H_{S\ MODE}$, $H_{S\ SD}$, $H_{S\ 25}$, and $H_{S\ 75}$ along the transect, with $H_{S\ MEAN} = 0.9–1.0$ m in predominantly FYI, and $H_{S\ MEAN} = 1.0–1.3$ m in predominantly MYI.
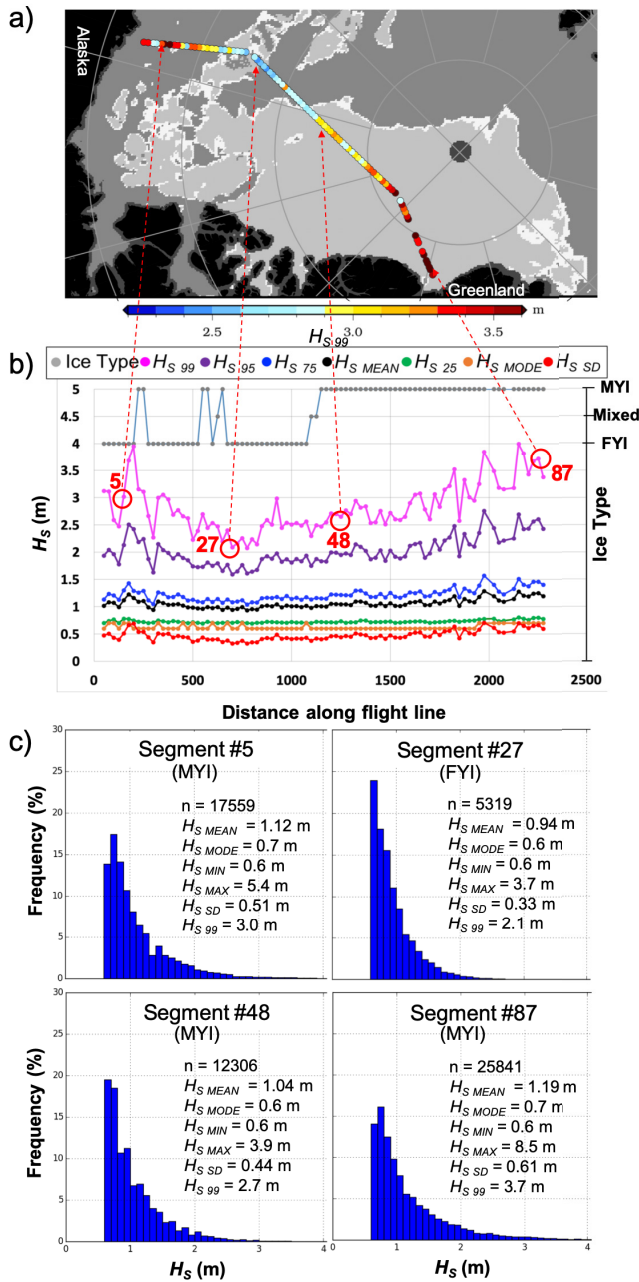
Fig. 2. (a) Transition between sea ice types along the OIB "Laxon Line" flight on April 20, 2016, where OSI SAF data (background) show the location of predominantly FYI (medium gray), predominantly MYI (light gray), and mixed ice types (white). (b) Sail height statistics at 25 km intervals along the flight line highlight the changes in parameter magnitude across differing ice types, including $H_{S\ SD}$ (red line), $H_{S\ MODE}$ (orange line), $H_{S\ 25}$ (green line), $H_{S\ MEAN}$ (blue line), and $H_{S\ 75}$ (black line), $H_{S\ 95}$ (purple line) and $H_{S\ 99}$ (magenta line), and ice type (gray dotted line). (c) Distributions and associated statistics corresponding to distinct 25 km intervals along the transect (red circles and numbers in (b)) show changes in the shape and tail of the distribution with changing ice type.

The magnitude of $H_{S\ 95}$ and $H_{S\ 99}$, however, showed larger variability with respect to ice type along the transect; $H_{S\ 99}$ varied from 2.2 to 3.0 m in predominantly FYI and from 2.5 to 4.0 m in predominantly MYI. A gradual increase in $H_{S\ 95}$ and $H_{S\ 99}$ is also observed as the transect approaches Greenland, where ice tends to be compressed against the coastline.

We examined the shape of the H_S distributions for four individual segments [Fig. 2(c)]. Segment 5 was located amongst MYI floes in the Beaufort Sea, segment 27 was entirely in FYI, segment 48 in the CA was in the MYI zone, and segment 87 was in the thickest MYI north of Greenland. Segment 27 had a $H_{S\ 99}$ of 2.1 m and a $H_{S\ MAX}$ of 3.7 m, while segments 5, 48, and 87, located in predominantly MYI, had distributions with longer tails and higher values of $H_{S\ 99}$ (2.7–3.4 m) and $H_{S\ MAX}$ (3.9–8.5 m).

The results from this transect are consistent with the analysis of the other flight lines. They support the initial findings of [8], who found that ridges formed in areas of predominantly MYI had larger sail heights than those formed in areas of predominantly FYI. As illustrated in Fig. 2(b) and (c), the principal differences in sail height with respect to ice type occur within the tails of the distributions, and there is very little variability in $H_{S\ MEAN}$ and $H_{S\ MODE}$ observed across the transect. The latter is to be expected since the $H_{S\ MEAN}$ and $H_{S\ MODE}$ statistics encompass the full height range of surface features, spanning small amplitude, e.g., older, weathered deformation features, to large amplitude features, e.g., pressure ridges. H_S associated with the tails of the distributions (i.e., $H_S \geq H_{S\ 95}$), on the other hand, is a better indicator of the predominant ice type in which the pressure ridge is found.

V. VARIABILITY IN ARCTIC SAIL HEIGHTS IN LATE WINTER

Next, we consider H_S characteristics derived for all OIB sea ice flights completed in the late winter during the nine-year study period. Statistics were determined from sail height distributions computed for contiguous, 25-km along-track segments. Following the results presented in Section IV, we primarily focus on $H_{S\ 99}$. OIB flights, separated by day, were paired with the daily OSI-403-c ice-type mask for the same date to delineate results by ice type. Only DMS images that were clearly within either the FYI or MYI cover were used, while images located in a mixture of ice types were not included.

Fig. 3 shows year-to-year variations in $H_{S\ 99}$ across the western Arctic Ocean between 2010 and 2018, along the flight line transects. First, we consider variability in two distinct geographical regions: the Beaufort/Chukchi (BC) and the CA, as previously defined in [13] and located by the magenta- and green-dashed lines in Fig. 3. For illustrative purposes, ice type is shown for the 30th March each year (approximate midpoint of annual OIB surveys). The spatial pattern of $H_{S\ 99}$ indicates that the largest sail heights were in the CA, where the most consolidated MYI is located close to the Canadian Arctic Archipelago and northern Greenland. Comparatively, smaller sails were found in the BC, an area of predominantly FYI.

Annual sail height distributions are shown in Fig. 4(a), illustrating statistical results differentiated by region regardless of ice-type designation. Over the nine-year period, H_S ranged 0.62–2.82 m ($H_{S\ 5}$ to $H_{S\ 99}$), and $H_{S\ MEAN}$ was 0.98 m, differing by ≤ 0.1 m between the two regions. $H_{S\ 99}$, however, averaged 2.1 m in the BC compared with 2.4 m in the CA, a difference of 0.3 m. $H_{S\ 99}$ in the BC was approximately equal to that in the CA in 2010 and 2018, but larger differences
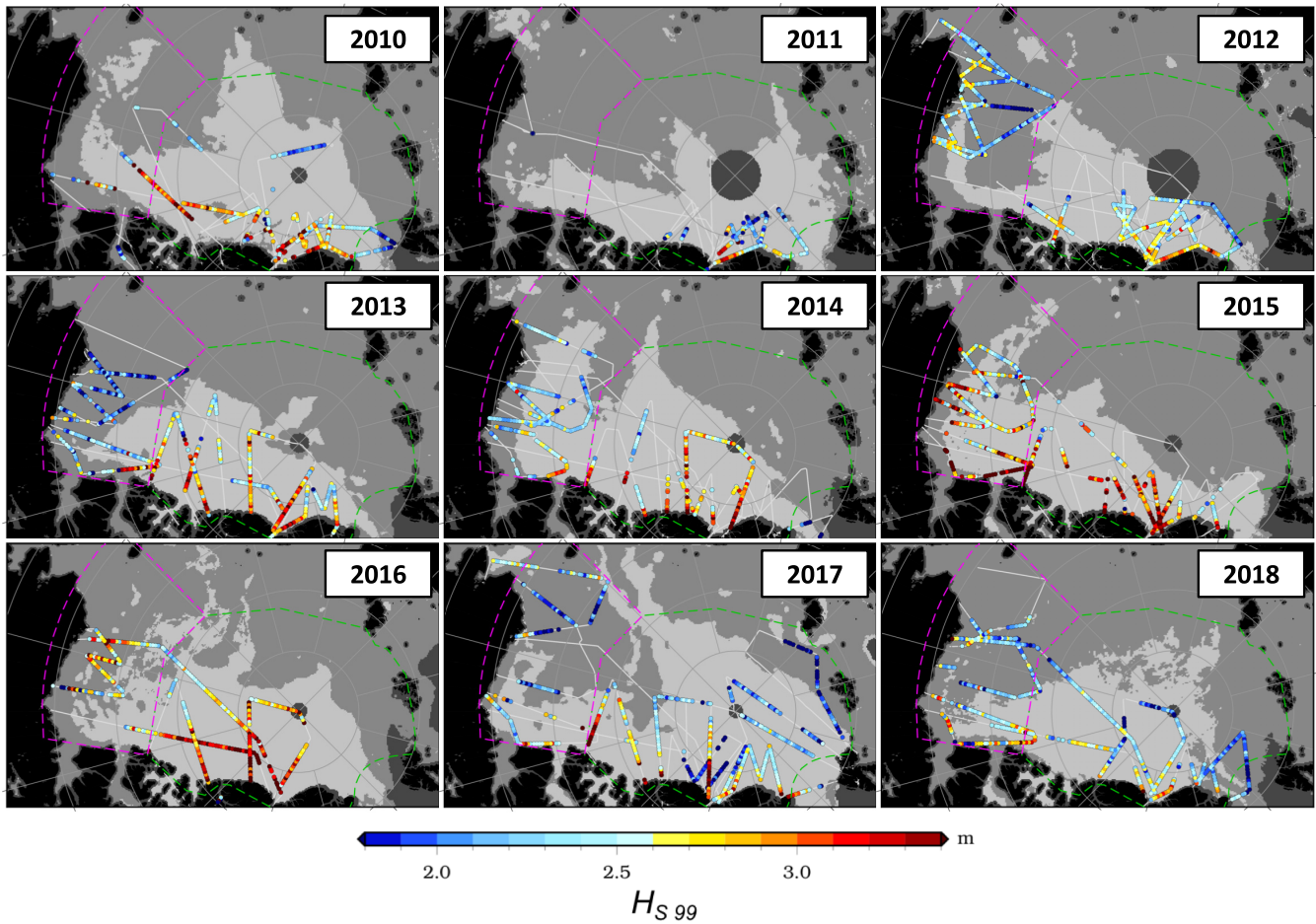
Fig. 3. Arctic sail height, as characterized by $H_{S\,99}$, at the end of the winter growth period, for 2010–2018. Ice type on March 30 of each year shows the location of predominantly FYI (medium gray) and predominantly MYI (light gray) [14]. The BC and CA regions are outlined by dashed magenta and green lines, respectively. Thin white lines represent the annual OIB flight lines.

in $H_{S\,99}$ occurred between the two regions from 2012 to 2017. In 2010, $H_{S\,99}$ was above average in both the BC and CA, followed by a decline in 2011. $H_{S\,99}$ then increased and peaked in 2015 in both the BC and CA, at 2.35 and 2.82 m, respectively. $H_{S\,99}$ remained anomalously high in 2016, after which it dropped to at or below average conditions in 2017 and 2018.

Next, we consider H_S variability as a function of ice-type classification, regardless of region. Fig. 4(b) distinguishes sail height distributions associated with ridges formed within predominately FYI from those that formed within predominately MYI. Over the nine-year period, $H_{S\,99}$ averaged 2.01 m for FYI compared with 2.41 m for MYI, a difference of 0.4 m. Interannual variability in H_S with respect to ice type is remarkably similar to interannual variability when H_S is delineated by region [Fig. 4(a)]. Yearly changes in H_S in FYI and MYI follow the same general pattern during the study period, with the largest sail heights occurring in 2015 and 2016, after which H_S in both FYI and MYI decreased. This observed interannual variability suggests that regional deformation in the ice cover at the end of winter increased from 2011 to 2016 and decreased in the subsequent years. Based on the general ice circulation patterns observed in the Arctic Ocean, after 2016, the most

heavily deformed sea ice may have drifted outside of the OIB sampling area and potentially exited the CA Ocean. In their recent study of ice export from the Arctic for the period 2010–2017, [14] found that over half of the MYI exported through the Fram Strait occurred in the winter (November–April) of 2016/2017.

To further examine differences in the tails of the sail height distributions, in the context of both region and ice type, we consider $H_{S\,99}$ averaged over 2010–2018 [Fig. 4(c)]. Results are shown on a log-linear scale for ridges formed in the BC and CA regions, as well as for those that formed in predominantly FYI and MYI. This step in the analysis reveals that the distribution of $H_{S\,99}$ differs by region and ice type. Modal values of $H_{S\,99}$ are ~0.4 m larger in the CA than in the BC region. We see little difference between $H_{S\,99\,CA}$ and $H_{S\,99\,MYI}$. This result is explained by the fact that the CA contains mainly MYI [Fig. 4(a), and also because the OIB flights within the CA focused on sampling the MYI cover (e.g., 2010–2016, Fig. 3]. There is a slight deviation between $H_{S\,99\,BC}$ and $H_{S\,99\,FYI}$, where $H_{S\,99\,BC}$ is larger than $H_{S\,99\,FYI}$. Although the BC region is predominantly FYI [Fig. 4(a), there is interannual variability in the percentage of MYI Figs. 3 and 4(a)], altering the regional $H_{S\,99}$ distribution.
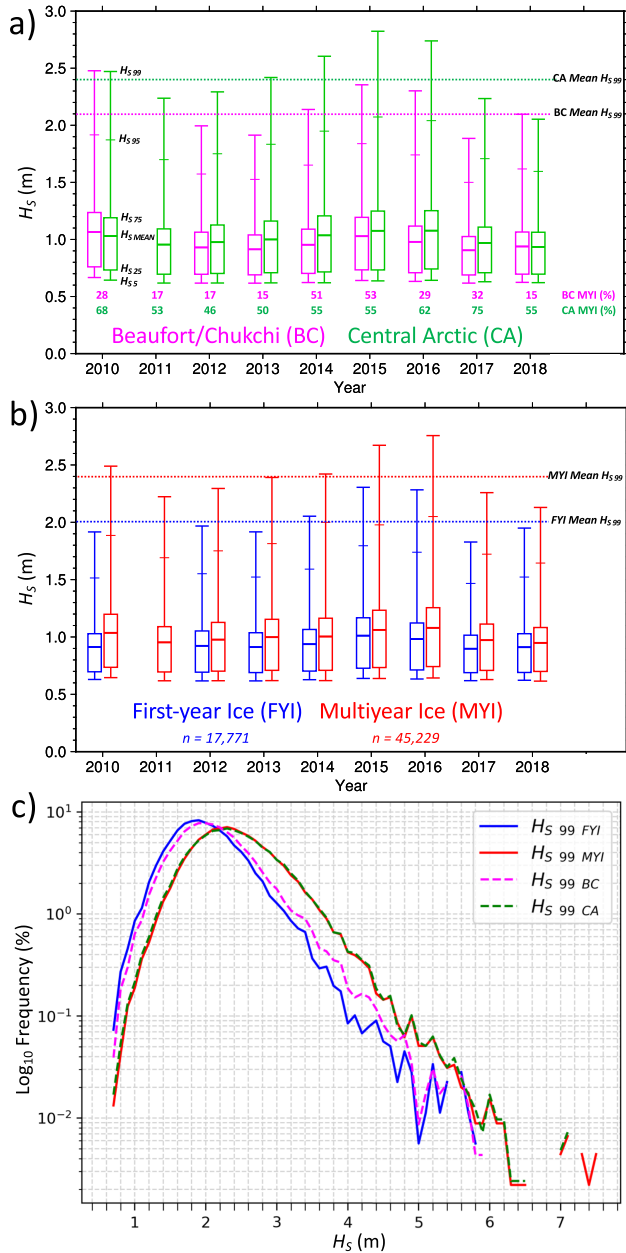
Fig. 4. End-of-winter sail height distributions for the period 2010–2018. (a) Box and whisker plot of interannual variability in H_S, distinguished by geographical area showing data within the BC region (magenta) and the CA region (green). The nine-year average in $H_{S\,99}$ is also shown (dotted lines). The relative MYI% is provided for both regions, by year. (b) Same as for (a) but with H_S distinguished by ice type showing ridges formed within predominantly FYI (blue) and predominantly MYI (red). (c) Log-linear plots of the nine-year average in $H_{S\,99}$ for the BC, CA, FYI, and MYI areas. (Note: no data available over FYI in 2011.)

VI. CONCLUSION

High-resolution optical imagery, acquired during late winter OIB flights over the Arctic Ocean, can be effectively used to determine the height of pressure ridge sails in the sea ice cover. By applying this technique for the period 2010–2018, we find a clear difference in the sail height distribution when we compare results in the CA to the BC seas regions. The regional results suggest that H_S is related to the dominant ice type within which the ridge formed. The tail of the sail height distributions (i.e., where $H_S \geq H_{S\,95}$), rather than

$H_{S\,MEAN}$, is a strong indicator of the predominant ice type where the ridge formed. $H_{S\,99}$ is, on average, ∼15% larger in the CA than in the BC region. Sail heights for ridges formed within predominantly MYI are ∼20% larger than those formed within predominantly FYI, both in terms of mean and modal value. Our analysis of the interannual and regional variability in H_S provides insight into the history of sea ice deformation in the western Arctic during the last decade and will help advance parameterizations of pressure ridges in sea ice models. The methods used in this study can be applied to other optical imagery including high-resolution national technical means (NTM) and WorldView satellite imagery acquired over the ice-covered ocean, to further extend regional and temporal coverage.

REFERENCES

[1] R. R. Parmerter and M. D. Coon, "Model of pressure ridge formation in sea ice," *J. Geophys. Res.*, vol. 77, no. 33, pp. 6565–6575, Nov. 1972.

[2] S. P. S. Arya, "Contribution of form drag on pressure ridges to the air stress on Arctic ice," *J. Geophys. Res.*, vol. 78, no. 30, pp. 7092–7099, Oct. 1973.

[3] D. A. Rothrock, "The energetics of the plastic deformation of pack ice by ridging," *J. Geophys. Res.*, vol. 80, no. 33, pp. 4514–4519, Nov. 1975, doi: 10.1029/JC080i033p04514.

[4] G. Spreen, R. Kwok, and D. Menemenlis, "Trends in Arctic sea ice drift and role of wind forcing: 1992–2009," *Geophys. Res. Lett.*, vol. 38, 2011, Art. no. L19501, doi: 10.1029/2011GL048970.

[5] W. D. Hibler and S. F. Ackley, "Height variation along sea ice pressure ridges and probability of finding, 'holes' for vehicle crossings," *J. Terramech.*, vol. 12, nos. 3–4, pp. 191–199, 1975, doi: 10.1016/0022-4898(75)90029-4).

[6] I. Zakharov, P. Bobby, D. Power, S. Warren, and M. Howell, "Detection and characterization of extreme ice features in single high resolution satellite imagery," in *Proc. IEEE Geosci. Remote Sens. Symp.*, Quebec City, QC, Canada, Jul. 2014, pp. 3965–3968, doi: 10.1109/IGARSS.2014.6947353.

[7] X. Miao, H. Xie, S. F. Ackley, and S. Zheng, "Object-based arctic sea ice ridge detection from high-spatial-resolution imagery," *IEEE Geosci. Remote Sens. Lett.*, vol. 13, no. 6, pp. 787–791, Jun. 2016.

[8] K. Duncan, S. L. Farrell, L. N. Connor, J. Richter-Menge, J. K. Hutchings, and R. Dominguez, "High-resolution airborne observations of sea-ice pressure ridge sail height," *Ann. Glaciol.*, vol. 59, no. 76, pp. 137–147, Jul. 2018, doi: 10.1017/aog.2018.2.

[9] L. Koenig, S. Martin, M. Studinger, and J. Sonntag, "Polar airborne observations fill gap in satellite data," *Eos, Trans. Amer. Geophys. Union*, vol. 91, no. 38, pp. 333–334, Sep. 2010, doi: 10.1029/2010EO380002.

[10] R. Dominguez, "IceBridge DMS L1B geolocated and orthorectified images," NASA Distrib. Active Arch. Center, Nat. Snow Ice Data Center, Boulder, CO, USA, User Guide, 2018, doi: 10.5067/OZ6VNOPMPRJ0.

[11] D. Lindell and D. Long, "Multiyear arctic ice classification using ASCAT and SSMIS," *Remote Sens.*, vol. 8, no. 4, p. 294, Mar. 2016, doi: 10.3390/rs8040294.

[12] S. Aaboe, L. A. Breivik, and S. Eastwood, "Global sea ice edge and type algorithm theoretical basis document," GBL SIE OSI-402-c GBL SIT OSI-403-c, EUMETSAT Ocean Sea Ice Satell. Appl. Facility, Lannion, France, Tech. Rep. 56, 2016. [Online]. Available: http://osisaf.met.no/p/ice//edge_type_long_description.html

[13] W. N. Meier, J. Stroeve, and F. Fetterer, "Whither A rctic sea ice? A clear signal of decline regionally, seasonally and extending beyond the satellite record," *Ann. Glaciol.*, vol. 46, pp. 428–434, 2007, doi: 10.3189/172756407782871170.

[14] R. Ricker, F. Girard-Ardhuin, T. Krumpen, and C. Lique, "Satellite-derived sea ice export and its impact on Arctic ice mass balance," *Cryosphere*, vol. 12, pp. 3017–3032, Sep. 2018, doi: 10.5194/tc-12-3017-2018.